2007

Numerical Methods for the Stochastic Landau-Lifshitz Navier-Stokes Equations

Alejandro Garcia, *San Jose State University*
John B Bell, *Lawrence Berkeley National Laboratory*
Sarah Williams, *University of California, Davis*

Numerical methods for the stochastic Landau-Lifshitz Navier-Stokes equations

John B. Bell,[1] Alejandro L. Garcia,[2] and Sarah A. Williams[3],*

[1]*Center for Computational Sciences and Engineering, Lawrence Berkeley National Laboratory, Berkeley, California 94720, USA*
[2]*Department of Physics, San Jose State University, San Jose, California 95192, USA*
[3]*Department of Mathematics, University of California, Davis, Davis, California 95616, USA*

The Landau-Lifshitz Navier-Stokes (LLNS) equations incorporate thermal fluctuations into macroscopic hydrodynamics by using stochastic fluxes. This paper examines explicit Eulerian discretizations of the full LLNS equations. Several computational fluid dynamics approaches are considered (including MacCormack's two-step Lax-Wendroff scheme and the piecewise parabolic method) and are found to give good results for the variance of momentum fluctuations. However, neither of these schemes accurately reproduces the fluctuations in energy or density. We introduce a conservative centered scheme with a third-order Runge-Kutta temporal integrator that does accurately produce fluctuations in density, energy, and momentum. A variety of numerical tests, including the random walk of a standing shock wave, are considered and results from the stochastic LLNS solver are compared with theory, when available, and with molecular simulations using a direct simulation Monte Carlo algorithm.

I. INTRODUCTION

Thermal fluctuations have long been a central topic of statistical mechanics, dating back to the light scattering predictions of Rayleigh (i.e., why the sky is blue) and the theory of Brownian motion of Einstein and Smoluchowski [1]. More recently, the study of fluctuations is an important topic in fluid mechanics due to the current interest in nanoscale flows, with applications ranging from microengineering [2–4] to molecular biology [5–7].

Microscopic fluctuations constantly drive a fluid from its mean state, making it possible to probe the transport properties by fluctuation dissipation. This is the basis for light scattering in physical experiments and Green-Kubo analysis in molecular simulations. Fluctuations are dynamically important for fluids undergoing phase transitions, nucleation, hydrodynamic instabilities, combustive ignition, etc., since the nonlinearities can exponentially amplify the effect of the fluctuations.

In molecular biology, the importance of fluctuations can be appreciated by noting that a typical molecular motor protein consumes adenosine triphosphate (ATP) at a power of roughly 10^{-16} W while operating in a background of 10^{-8} W of thermal noise power, which is likened to be "as difficult as walking in a hurricane is for us" [6]. While the randomizing property of fluctuations would seem to be unfavorable for the self-organization of living organisms, Nature has found a way to exploit these fluctuations at the molecular level. The second law of thermodynamics does not allow motor proteins to extract work from equilibrium fluctuations, yet the thermal noise actually assists the directed motion of the protein by providing the mechanism for overcoming potential barriers.

Following Nature's example, there is interest in the fabrication of nanoscale devices powered by [8] or constructed using [9] so-called "Brownian motors." Another application is in micro-total-analytical systems (μTAS) or "lab-on-a-chip" systems that promise single-molecule detection and analysis [10]. Specifically, the Brownian ratchet mechanism has been demonstrated to be useful for biomolecular separation [11,12] and simple mechanisms for creating heat engines driven by nonequilibrium fluctuations have been proposed [13,14].

The study of fluctuations in nanoscale fluids is particularly interesting when the fluid is under extreme conditions or near a hydrodynamic instability. Examples include the breakup of droplets in nanojets [15–17] and fluid mixing in the Rayleigh-Taylor instability [18,19]. Finally, exothermic reactions, such as in combustion and explosive detonation, can depend strongly on the nature of thermal fluctuations [20,21].

To incorporate thermal fluctuations into macroscopic hydrodynamics, Landau and Lifshitz introduced an extended form of the Navier-Stokes equations by adding stochastic flux terms [22]. The Landau-Lifshitz Navier-Stokes (LLNS) equations may be written as

$$\mathbf{U}_t + \boldsymbol{\nabla} \cdot \mathbf{F} = \boldsymbol{\nabla} \cdot \mathbf{D} + \boldsymbol{\nabla} \cdot \mathbf{S}, \tag{1}$$

where

$$\mathbf{U} = \begin{pmatrix} \rho \\ \mathbf{J} \\ E \end{pmatrix}$$

is the vector of conserved quantities (density of mass, momentum, and energy). The hyperbolic flux is given by

$$\mathbf{F} = \begin{pmatrix} \rho\mathbf{v} \\ \rho\mathbf{v}\mathbf{v} + P\mathbf{I} \\ \mathbf{v}E + P\mathbf{v} \end{pmatrix}$$

and the diffusive flux is given by

*Electronic address: sawilliams@math.ucdavis.edu

$$\mathbf{D} = \begin{pmatrix} 0 \\ \boldsymbol{\tau} \\ \boldsymbol{\tau} \cdot \mathbf{v} + \kappa \nabla T \end{pmatrix},$$

where $\mathbf{v}$ is the fluid velocity, P is the pressure, T is the temperature, and $\boldsymbol{\tau} = \eta(\nabla \mathbf{v} + \nabla \mathbf{v}^T - \frac{2}{3}\mathbf{I}\nabla \cdot \mathbf{v})$ is the stress tensor. Here η and κ are coefficients of viscosity and thermal conductivity, respectively, where we have assumed the bulk viscosity is zero.

The mass flux is microscopically exact but the other two flux components are not; for example, at molecular scales heat may spontaneously flow from cold to hot, in violation of the macroscopic Fourier law. To account for such spontaneous fluctuations, the LLNS equations include a stochastic flux

$$\mathbf{S} = \begin{pmatrix} 0 \\ \mathcal{S} \\ \mathcal{Q} + \mathbf{v} \cdot \mathcal{S} \end{pmatrix},$$

where the stochastic stress tensor $\mathcal{S}$ and heat flux $\mathcal{Q}$ have zero mean and covariances given by

$$\langle \mathcal{S}_{ij}(\mathbf{r},t)\mathcal{S}_{k\ell}(\mathbf{r}',t')\rangle = 2k_B\eta T\left(\delta_{ik}^K\delta_{j\ell}^K + \delta_{i\ell}^K\delta_{jk}^K - \frac{2}{3}\delta_{ij}^K\delta_{k\ell}^K\right)$$
$$\times \delta(\mathbf{r}-\mathbf{r}')\delta(t-t'),$$

$$\langle \mathcal{Q}_i(\mathbf{r},t)\mathcal{Q}_j(\mathbf{r}',t')\rangle = 2k_B\kappa T^2\delta_{ij}^K\delta(\mathbf{r}-\mathbf{r}')\delta(t-t'),$$

and

$$\langle \mathcal{S}_{ij}(\mathbf{r},t)\mathcal{Q}_k(\mathbf{r}',t')\rangle = 0,$$

where k_B is Boltzmann's constant. The LLNS equations have been derived by a variety of approaches (see [22–25]) and have even been extended to relativistic hydrodynamics [26]. While they were originally developed for equilibrium fluctuations (see Appendix A), specifically the Rayleigh and Brillouin spectral lines in light scattering, the validity of the LLNS equations for nonequilibrium systems has been derived [27] and verified in molecular simulations [28–30].

In this paper we investigate a variety of numerical schemes for solving the LLNS equations. For simplicity, we restrict our attention to one-dimensional systems, so Eq. (1) simplifies to

$$\frac{\partial}{\partial t}\begin{pmatrix} \rho \\ J \\ E \end{pmatrix} = -\frac{\partial}{\partial x}\begin{pmatrix} \rho u \\ \rho u^2 + P \\ (E+P)u \end{pmatrix} + \frac{\partial}{\partial x}\begin{pmatrix} 0 \\ \frac{4}{3}\eta\partial_x u \\ \frac{4}{3}\eta u\partial_x u + \kappa\partial_x T \end{pmatrix}$$
$$+ \frac{\partial}{\partial x}\begin{pmatrix} 0 \\ s \\ q + us \end{pmatrix}, \qquad (2)$$

where

$$\langle s(x,t)s(x',t')\rangle$$
$$= \frac{1}{\sigma^2}\int dy \int dy' \int dz \int dz' \langle \mathcal{S}_{xx}(\mathbf{r},t)\mathcal{S}_{xx}(\mathbf{r}',t')\rangle$$
$$= \frac{8k_B\eta T}{3\sigma}\delta(x-x')\delta(t-t')$$

and

$$\langle q(x,t)q(x',t')\rangle$$
$$= \frac{1}{\sigma^2}\int dy \int dy' \int dz \int dz' \langle \mathcal{Q}_x(\mathbf{r},t)\mathcal{Q}_x(\mathbf{r}',t')\rangle$$
$$= \frac{2k_B\kappa T^2}{\sigma}\delta(x-x')\delta(t-t')$$

with σ being the surface area of the system in the yz plane.

Furthermore, we take the fluid to be a dilute gas with equation of state $P=\rho RT$ and energy density $E=c_v\rho T + \frac{1}{2}\rho u^2$. The transport coefficients are only functions of temperature; for example, for a hard sphere gas $\eta = \eta_0\sqrt{T}$ and $\kappa = \kappa_0\sqrt{T}$, where η_0 and κ_0 are constants. The numerical schemes developed in this paper may readily be formulated for other fluids. Our choice is motivated by a desire to compare with molecular simulations (see Appendix B) of a monatomic, hard sphere gas (for which $R=k_B/m$ and $c_v = \frac{R}{\gamma-1}$ where m is the mass of a particle and the ratio of specific heats is $\gamma = \frac{5}{3}$).

Several numerical approaches for the Landau-Lifshitz Navier-Stokes (LLNS) equations, and related stochastic hydrodynamic equations, have been proposed. The most successful is a stochastic lattice-Boltzmann model developed by Ladd for simulating solid-fluid suspensions [31]. This approach for modeling the Brownian motion of particles was adopted by Sharma and Patankar [32] using a finite difference scheme that incorporates a stochastic momentum flux into the *incompressible* Navier-Stokes equations. By including the stochastic stress tensor of the LLNS equations into the lubrication equations Moseler and Landman [15] obtain good agreement with their molecular dynamics simulation in modeling the breakup of nanojets; recent extensions of this work confirm the important role of fluctuations and the utility of the stochastic hydrodynamic description [16,17]. An alternative mesoscopic approach to computational fluid dynamics, based on a stochastic description defined by a discrete master equation, is proposed by Breuer and Petruccione [33,34]. They show that the structure of the resulting system recovers the fluctuations of LLNS.

Serrano and Español [35] describe a finite volume Lagrangian discretization of the continuum equations of hydrodynamics using Voronoi tessellation. Casting their model into the GENERIC structure [36] allows for the introduction of thermal fluctuations yielding a consistent discrete model for Lagrangian fluctuating hydrodynamics. De Fabritiis and co-workers [37,38] derive a similar mesoscopic, Voronoi-based algorithm using the dissipative particle dynamics (DPD) method. The dissipative particles follow the dynamics of extended objects subject to hydrodynamic forces, with stresses and heat fluxes given by the LLNS equations.

In earlier work Garcia *et al.* [39] developed a simple finite difference scheme for the linearized LLNS equations. Though successful, that scheme was custom-designed to solve a specific problem; it cannot be extended readily, since it relies on special assumptions of zero net flow and constant heat flux and would be unstable in the more general case. Related finite difference schemes have been demonstrated for the diffusion equation [40], the "train" model [41], and the stochastic Burgers' equation [42], specifically in the context of adaptive mesh and algorithm refinement hybrids that couple particle and continuum algorithms. De Fabritiis and co-workers [43,44] present a related approach of using algorithm refinement to couple molecular dynamics simulations to numerical algorithms for the stochastic hydrodynamic equations. Their formulation assumes isothermal conditions and uses a simple Euler scheme for the stochastic partial differential equations (PDEs).

In the next section we develop three stochastic PDE schemes based on standard computational fluid dynamics (CFD) schemes for compressible flow. The schemes are tested in a variety of scenarios in Secs. III and IV, measuring spatial and time correlations at equilibrium and away from equilibrium. Results are compared to theoretically derived values, and also to results from direct simulation Monte Carlo (DSMC) particle simulations (see Appendix B). We also examine the influence of fluctuations on shock drift, comparing results from the LLNS solver with DSMC simulations. The concluding section summarizes the results and discusses future work, with an emphasis on the issues related to using the resulting methodology as the foundation for a hybrid algorithm.

II. NUMERICAL METHODS

The goal here is to develop an Eulerian discretization of the full LLNS equations, representing an extension of the approach discussed in [42] to compressible flow. We restrict consideration here to finite-volume schemes in which all of the variables are collocated, so that the resulting method can form the basis of a hybrid method in which a particle description (e.g., DSMC) is coupled to the LLNS discretization. Within this class of discretizations, our aim is to recover the correct fluctuating statistics. In this section we first develop two methods based on CFD schemes that are commonly used for the Navier-Stokes equations. These schemes turn out not to produce the correct fluctuation intensities, leading us to introduce a specialized centered Runge-Kutta scheme.

A. MacCormack scheme

Based on the success of the simple second-order scheme in [39], we first consider MacCormack's variant of two-step Lax-Wendroff for solving fluctuating LLNS. (A standard version of two-step Lax-Wendroff was also considered with similar but slightly poorer results.) The MacCormack method is applied in the following way:

$$\mathbf{U}_j^* = \mathbf{U}_j^n - \frac{\Delta t}{\Delta x}(\mathbf{F}_j^n - \mathbf{F}_{j-1}^n) + \frac{\Delta t}{\Delta x}(\mathbf{D}_{j+1/2}^n - \mathbf{D}_{j-1/2}^n)$$

$$+ \frac{\Delta t}{\Delta x}(\widetilde{\mathbf{S}}_{j+1/2}^n - \widetilde{\mathbf{S}}_{j-1/2}^n),$$

$$\mathbf{U}_j^{**} = \mathbf{U}_j^* - \frac{\Delta t}{\Delta x}(\mathbf{F}_{j+1}^* - \mathbf{F}_j^*) + \frac{\Delta t}{\Delta x}(\mathbf{D}_{j+1/2}^* - \mathbf{D}_{j-1/2}^*)$$

$$+ \frac{\Delta t}{\Delta x}(\widetilde{\mathbf{S}}_{j+1/2}^* - \widetilde{\mathbf{S}}_{j-1/2}^*),$$

$$\mathbf{U}_j^{n+1} = \frac{1}{2}(\mathbf{U}_j^n + \mathbf{U}_j^{**}).$$

Here $\mathbf{D}_{j+1/2}^n$ is a simple finite difference approximation to $\mathbf{D}$ and

$$\widetilde{\mathbf{S}}_{j+1/2} = \sqrt{2}\mathbf{S}_{j+1/2} = \sqrt{2}\begin{pmatrix} 0 \\ s_{j+1/2} \\ q_{j+1/2} + u_{j+1/2}s_{j+1/2} \end{pmatrix}.$$

The approximation to the stochastic stress tensor, $s_{j+1/2}$, is computed as

$$s_{j+1/2} = \sqrt{\frac{4k_B}{3\Delta t V_c}(\eta_{j+1}T_{j+1} + \eta_j T_j)}\,\mathcal{R}_{j+1/2} \qquad (3)$$

where V_c is the volume of a cell and the $\mathcal{R}$'s are independent, Gaussian distributed random values with zero mean and unit variance. The approximation to the discretized stochastic heat flux, $q_{j+1/2}$, is evaluated as

$$q_{j+1/2} = \sqrt{\frac{k_B}{\Delta t V_c}[\kappa_{j+1}(T_{j+1})^2 + \kappa_j(T_j)^2]}\,\mathcal{R}_{j+1/2}. \qquad (4)$$

These same stochastic flux approximations are used in all three continuum methods presented here.

For a predictor-corrector type scheme, such as two-step MacCormack, the variance in the stochastic flux at $j+1/2$ is given by

$$\langle(\widetilde{\mathbf{S}}_{j+1/2}^\Sigma)^2\rangle = \left\langle\left(\frac{1}{2}\widetilde{\mathbf{S}}_{j+1/2}^n + \frac{1}{2}\widetilde{\mathbf{S}}_{j+1/2}^*\right)^2\right\rangle$$

$$= \left(\frac{1}{2}\right)^2\langle(\widetilde{\mathbf{S}}_{j+1/2}^n)^2\rangle + \left(\frac{1}{2}\right)^2\langle(\widetilde{\mathbf{S}}_{j+1/2}^*)^2\rangle.$$

Neglecting for the moment the multiplicity of the noise (i.e., taking $T^n = T^*$) then

$$\langle(\widetilde{\mathbf{S}}_{j+1/2}^\Sigma)^2\rangle = \frac{1}{2}\langle(\widetilde{\mathbf{S}}_{j+1/2}^n)^2\rangle = \langle(\mathbf{S}_{j+1/2}^n)^2\rangle$$

which is the correct result. Note that later we will find that the multiplicity of the noise is generally weak for the LLNS equations (see Sec. III A).

B. Piecewise parabolic method

In [42] a piecewise linear second-order Godunov scheme was shown to be effective for solving the fluctuating Burgers' equation. We considered two versions of higher-order Godunov methods for the LLNS, a piecewise linear version [45], and the piecewise parabolic method (PPM) introduced in [46]. The PPM algorithm, based on the direct Eulerian version presented in [47], produced considerably better results than the piecewise linear scheme. Since our goal is to

preserve fluctuations, we do not limit slopes and we do not include discontinuity detection in the algorithm.

For this scheme the hyperbolic terms of the LLNS equations are considered in terms of hydrodynamic and local characteristic variables. In hydrodynamic variables we have

$$\frac{\partial}{\partial t}\mathbf{V} + \mathbf{A}\frac{\partial}{\partial x}\mathbf{V} = 0,$$

where

$$\mathbf{V}_j = \begin{pmatrix} \rho_j \\ u_j \\ P_j \end{pmatrix}.$$

The local characteristic variables are interpolated via a fourth-order scheme to the left $(-)$ and right $(+)$ edges of each cell:

$$\mathbf{W}_{j,\pm}^n = \frac{7}{12}(\mathbf{L}_j\mathbf{V}_j + \mathbf{L}_j\mathbf{V}_{j\pm1}) - \frac{1}{12}(\mathbf{L}_j\mathbf{V}_{j\mp1} + \mathbf{L}_j\mathbf{V}_{j\pm2}),$$

where $\mathbf{L}_j$ is the matrix whose rows are the left eigenvectors of $\mathbf{A}$ evaluated at $\mathbf{V}_j$.

These values, together with the cell-centered value $\mathbf{W}_j^n = \mathbf{L}_j\mathbf{V}_j$, are used to construct a parabolic profile $\mathbf{W}_{j,k}(\theta)$ for each characteristic variable k in each cell,

$$\mathbf{W}(\theta) = \mathbf{W}_{j,-} + \theta \left[\mathbf{W}_j + \theta(1 - \theta)\mathbf{W}_{j6} \right],$$

where

$$\theta = \frac{x - (j - 1/2)\ x}{x},$$

$$\mathbf{W}_j^n = \mathbf{W}_{j,+}^n - \mathbf{W}_{j,-}^n,$$

and

$$\mathbf{W}_{j6}^n = 6\left(\mathbf{W}_j^n - \frac{1}{2}(\mathbf{W}_{j,+}^n + \mathbf{W}_{j,-}^n)\right).$$

Time-centered updates are based on the sign of each local characteristic wave speed, $\lambda_{j,k}$:

$$\mathbf{W}_{j,\pm,k}^{n+1/2} = \begin{cases} \frac{1}{\nu_{j,k}} \int_{\pm1/2-\nu_{j,k}}^{\pm1/2} \mathbf{W}_{j,k}(\theta)d\theta, & \pm\lambda_{j,k} > 0 \\ \mathbf{W}_{j,\pm,k}^n & \text{otherwise.} \end{cases},$$

where $\nu_{j,k} = \lambda_{j,k}\frac{t}{x}$.

Finally, the time-centered values are transformed back into primitive variables and used as inputs to a Riemann problem at each cell edge. We use the approximate Riemann solver discussed in [48]. This approach iterates the phase-space solution in the u-p plane, approximating the rarefaction curves by the Hugoniot locus. The overall approach is able to handle strong discontinuities and is second-order in wave strength.

Approximations to the viscous and stochastic flux terms are discussed in Sec. II A. For our PPM algorithm we center the viscous update in time, so that the complete update is as follows:

$$\mathbf{U}_j^* = \mathbf{U}_j^n - \frac{t}{x}\mathbf{F}_j^n + \frac{t}{x}(\mathbf{D}_j^n + \widetilde{\mathbf{S}}_j^n),$$

$$\mathbf{U}_j^{n+1} = \mathbf{U}_j^n - \frac{t}{x}\mathbf{F}_j^n + \frac{1}{2}\left(\frac{t}{x}\right)(\mathbf{D}_j^n + \widetilde{\mathbf{S}}_j^n + \mathbf{D}_j^* + \widetilde{\mathbf{S}}_j^*).$$

As discussed in Sec. II A, for the PPM scheme we use the stochastic flux approximation $\widetilde{\mathbf{S}}_j = \sqrt{2}\mathbf{S}_j$, since the averaging in the time-centering reduces the variance in the flux by half.

C. Variance-preserving third-order Runge-Kutta method

Equilibrium tests, presented in detail in Sec. III A, show that neither of the traditional numerical methods with stochastic flux discussed above accurately represents the fluctuations in the LLNS equations. The principal difficulty arises because there is no stochastic forcing term in the mass conservation equation. Accurately capturing density fluctuations requires that the fluctuations be preserved in computing the mass flux. Another key observation is that the representation of fluctuations in the above schemes is also sensitive to the time step, with extremely small time steps leading to improved results. This suggests that temporal accuracy also plays a significant role in capturing fluctuations. Based on these observations we have developed a discretization aimed specifically at capturing fluctuations in the LLNS equations. The method is based on a third-order, total variation diminishing (TVD) Runge-Kutta temporal integrator (RK3) [49,50] combined with a centered discretization of hyperbolic and diffusive fluxes. The rationale for selecting an RK3 temporal integration scheme is not based on higher-order accuracy considerations; in fact, we expect significant limitation in the order of accuracy for any scheme applied to a stochastic differential equation [51]. Instead the motivation here is one of robustness. A simple forward Euler scheme would be unstable because there is no dissipation term in the continuity equation. Similarly, since the optimal second-order TVD RK method (Heun's method) is unstable for operators with pure imaginary spectra, it is also an unsuitable choice for the system considered here.

The RK3 discretizaton can be written in the following three-stage form:

$$\mathbf{U}_j^{n+1/3} = \mathbf{U}_j^n - \frac{t}{x}(\mathcal{F}_{j+1/2}^n - \mathcal{F}_{j-1/2}^n),$$

$$\mathbf{U}_j^{n+2/3} = \frac{3}{4}\mathbf{U}_j^n + \frac{1}{4}\mathbf{U}_j^{n+1/3} - \frac{1}{4}\left(\frac{t}{x}\right)(\mathcal{F}_{j+1/2}^{n+1/3} - \mathcal{F}_{j-1/2}^{n+1/3}),$$

$$\mathbf{U}_j^{n+1} = \frac{1}{3}\mathbf{U}_j^n + \frac{2}{3}\mathbf{U}_j^{n+2/3} - \frac{2}{3}\left(\frac{t}{x}\right)(\mathcal{F}_{j+1/2}^{n+2/3} - \mathcal{F}_{j-1/2}^{n+2/3}),$$

where $\mathcal{F} = -\mathbf{F} + \mathbf{D} + \widetilde{\mathbf{S}}$. Combining the three stages, we can write

$$\mathbf{U}_j^{n+1} = \mathbf{U}_j^n - \frac{t}{x}\left(\frac{1}{6}(\mathcal{F}_{j+1/2}^n - \mathcal{F}_{j-1/2}^n) + \frac{1}{6}(\mathcal{F}_{j+1/2}^{n+1/3} - \mathcal{F}_{j-1/2}^{n+1/3})\right.$$

$$\left. + \frac{2}{3}(\mathcal{F}_{j+1/2}^{n+2/3} - \mathcal{F}_{j-1/2}^{n+2/3})\right).$$

The variance in the stochastic flux at $j+1/2$ is given by

$$\langle(\mathbf{S}_{j+1/2})^2\rangle = \left\langle\left(\frac{1}{6}(\widetilde{\mathbf{S}}_{j+1/2}^0) + \frac{1}{6}(\widetilde{\mathbf{S}}_{j+1/2}^{1/3}) + \frac{2}{3}(\widetilde{\mathbf{S}}_{j+1/2}^{2/3})\right)^2\right\rangle$$

$$= \left(\frac{1}{6}\right)^2\langle(\widetilde{\mathbf{S}}_{j+1/2}^0)^2\rangle + \left(\frac{1}{6}\right)^2\langle(\widetilde{\mathbf{S}}_{j+1/2}^{1/3})^2\rangle$$

$$+ \left(\frac{2}{3}\right)^2\langle(\widetilde{\mathbf{S}}_{j+1/2}^{2/3})^2\rangle.$$

Again, neglecting the multiplicity in the noise we obtain the desired result that $\langle(\mathbf{S})^2\rangle = \frac{1}{2}\langle(\widetilde{\mathbf{S}})^2\rangle = \langle(\mathbf{S})^2\rangle$, that is, taking $\widetilde{\mathbf{S}} = \sqrt{2}\mathbf{S}$ corrects for the reduction of the stochastic flux variance due to the three-stage averaging of the fluxes. However, this treatment does not directly affect the fluctuations in density, since the component of $\mathbf{S}$ is zero in the continuity equation. To compensate for the suppression of density fluctuations due to the temporal averaging we interpolate the momentum J (and the other conserved quantities) from cell-centered values:

$$J_{j+1/2} = \alpha_1(J_j + J_{j+1}) - \alpha_2(J_{j-1} + J_{j+2}), \quad (5)$$

where

$$\alpha_1 = (\sqrt{7} + 1)/4 \quad \text{and} \quad \alpha_2 = (\sqrt{7} - 1)/4. \quad (6)$$

Then in the case of constant J we have exactly $J_{j+1/2} = J$ and $\langle\delta J_{j+1/2}^2\rangle = 2\langle\delta J^2\rangle$, as desired; the interpolation is consistent and compensates for the variance-reducing effect of the multistage Runge-Kutta algorithm. The interpolation formula is similar to the PPM spatial construction except in the PPM construction $\alpha_1 = 7/12$ and $\alpha_2 = 1/12$. Tests based on these alternative weights produced results intermediate to the RK3 scheme and the PPM scheme. We also considered interpolation of primitive variables but found that interpolation based on primitive variables led to stable but undamped oscillatory behavior. Finally, the diffusive terms $\mathbf{D}$ are discretized with standard second-order finite difference approximations.

D. Boundary conditions

In Secs. III and IV we consider test problems for the various PDE algorithms on either a periodic computational domain, a computational domain bounded by thermal walls, or a computational domain bounded by infinite reservoirs. Boundary conditions are implemented using ghost cells. For the periodic and reservoir boundaries, it is straightforward to determine the ghost cell data.

For thermal wall boundaries, the treatment of the hyperbolic flux at the thermal wall varies by method. In MacCormack, conserved quantities are reflected across the boundaries of the domain. The temperature in the ghost cells is determined by linear extrapolation, and the no-flow condition is enforced by setting the velocity terms of the hyperbolic flux to zero within the ghost cells.

For thermal wall boundaries in PPM, ghost cells are populated by reflecting primitive variable values across the domain boundaries, and the temperature in the ghost cells is determined by linear extrapolation. The PPM routine takes as input the cell-centered primitive variable data and returns a Riemann solution at each cell edge. On the domain boundaries, we modify these Riemann solutions by enforcing fixed wall temperature (i.e., the pressure at the wall is taken to be a function of the fixed wall temperature) before computing the hyperbolic flux across each edge.

In RK3 we also employ a Riemann solver at thermal wall boundaries, which ensures that characteristic compatibility relations are respected at the physical boundaries. The Riemann solver requires primitive variable inputs from the interior and exterior of each physical boundary. Mass density at the interior of the boundary is estimated by populating ghost cells (by reflection of ρ across the boundary of the domain), then interpolating onto the domain boundary [as in Eq. (5)]. The no-flow condition is enforced across the boundary, and pressure at the boundary is a function of the fixed wall temperature, T_L or T_R. The interior Riemann solver input for the left-hand domain boundary is therefore given by

$$\begin{bmatrix} \rho_{int} \\ u_{int} \\ P_{int} \end{bmatrix} = \begin{bmatrix} 2\alpha_1\rho_1 - 2\alpha_2\rho_2 \\ 0 \\ RT_L\rho_{int} \end{bmatrix},$$

where $\alpha_{1,2}$ are the interpolation coefficients given in Eq. (6), and R is the gas constant. The data for the right-hand boundary is similar. The input to the Riemann solver on the exterior side of the boundary is the reflection of the interior input data:

$$\begin{bmatrix} \rho_{ext} \\ u_{ext} \\ P_{ext} \end{bmatrix} = \begin{bmatrix} \rho_{int} \\ -u_{int} \\ P_{int} \end{bmatrix}.$$

The treatment of reservoir boundaries is similar. However, ghost cells are populated with reservoir data and the input to the Riemann problem on the exterior side of the boundary is the reservoir data.

For all the methods, to calculate the diffusive flux at the domain boundaries in the case of thermal walls we use a one-sided finite difference formulation to approximate u_x and T_x. These finite difference approximations use data at the domain boundaries (L and R) and at the centers of the first two interior cells on either side of the domain:

$$T_x|_L = \frac{9T_1 - T_2 - 8T_L}{3\,x} + O(\,x^2),$$

$$T_x|_R = -\frac{9T_n - T_{n-1} - 8T_R}{3\,x} + O(\,x^2),$$

and

$$u_x|_L = \frac{9u_1 - u_2 - 8u_L}{3\,x} + O(\,x^2),$$

TABLE I. System parameters (in cgs units) for simulations of a dilute gas in a periodic domain.

Molecular diameter (argon)	3.66×10^{-8}
Molecular mass (argon)	6.63×10^{-23}
Reference mass density	1.78×10^{-3}
Reference temperature	273
Sound speed	30 781
Specific heat c_v	3.12×10^6
System length	1.25×10^{-4}
Reference mean free path	6.26×10^{-6}
System volume	1.96×10^{-16}
Time step	1.0×10^{-12}
Number of cells	40
Number of samples	10^7
Number of particles	5265
Collision grid size	3.13×10^{-6}

$$u_{x\,R} = -\frac{9u_n - u_{n-1} - 8u_R}{3\,x} + O(\,x^2).$$

III. NUMERICAL TESTS—EQUILIBRIUM

This section presents results from a variety of scenarios in which the three schemes described above were tested. The physical domain is chosen to be compatible with DSMC particle simulations; see Table I for the system's parameters and Appendix B for a description of DSMC. The domain is partitioned into 40 cells of equal size x and hyperbolic and diffusive stability constraints determine the maximum time step t:

$$(|u + c_s|)\frac{t}{x} \leqslant 1,$$

$$\max\left(\frac{4}{3}\frac{\bar{\eta}}{\bar{\rho}}, \frac{\bar{\kappa}}{\bar{\rho}c_v}\right)\frac{t}{x^2} \leqslant \frac{1}{2},$$

where the sound speed $c_s = \sqrt{\gamma \bar{P}/\bar{\rho}}$, $\bar{\eta} = \eta(\bar{T})$, and $\bar{\kappa} = \kappa(\bar{T})$; the overline indicates reference values (e.g., equilibrium values around which the system fluctuates). For the reference state (argon at STP) and a cell width of $x \approx 10^{-6}$ cm the time step used was $t = 10^{-12}$ s. Note that for these parameters the number of molecules per cell is approximately 100 so the thermal fluctuations will be of significant magnitude.

A. Variances at equilibrium

The first benchmark for our numerical schemes is recovering the correct variance of fluctuations for a system at equilibrium. For this initial test problem, we take a periodic domain with zero net flow and constant average density and temperature. Similar results, not presented here, were obtained for the case of constant nonzero net flow. The variances are computed in 40 spatial cells from 10^7 samples and then averaged over the cells.

TABLE II. Variance in conserved quantities at equilibrium (computed values are accurate to approximately 0.1%).

	Computed value	Pct. error
$\langle \delta\rho^2 \rangle$ Exact value: 2.35×10^{-8}		
MacCormack scheme	2.01×10^{-8}	-14.3%
Piecewise parabolic method	1.97×10^{-8}	-16.0%
Third-order Runge-Kutta	2.32×10^{-8}	-1.3%
Molecular simulation (DSMC)	2.35×10^{-8}	0.0%
$\langle \delta J^2 \rangle$ Exact value: 13.34		
MacCormack scheme	13.31	-0.3%
Piecewise parabolic method	13.27	-0.5%
Third-order Runge-Kutta	13.65	2.3%
Molecular simulation (DSMC)	13.21	-1.0%
$\langle \delta E^2 \rangle$ Exact value: 2.84×10^{10}		
MacCormack scheme	2.61×10^{10}	-8.4%
Piecewise parabolic method	2.58×10^{10}	-9.4%
Third-order Runge-Kutta	2.87×10^{10}	0.9%
Molecular simulation (DSMC)	2.78×10^{10}	-2.1%

Table II compares the theoretical variances (see Appendix A) with those measured in the three stochastic PDE schemes and the DSMC particle simulation. The MacCormack and PPM schemes do a relatively poor job (8–16 % error) for the variances of density and energy. Better results can be obtained with PPM and MacCormack by dramatically decreasing the value of t. However, it is not desirable to run simulations at extremely small time step. Only the third-order Runge-Kutta integrator generates the correct variance of density and energy while advancing with time steps near the stability limit.

The stochastic flux in our numerical schemes for the LLNS equations is a multiplicative noise since we take variance to be a function of instantaneous temperature [see Eqs. (3) and (4)]. We tested the importance of the multiplicity of the noise by repeating the equilibrium runs with the temperature fixed in the stochastic fluxes and found no difference in the results. Earlier work [39] also showed that the multiplicity of the noise is quite weak. While this might not be the case for extreme conditions (e.g., extremely small cell volumes) at that point the hydrodynamic assumptions implicit in the construction LLNS PDEs would also break down. Note that since the fluxes are time-centered the scheme reproduces the representation of the Stratonovich integral [51,52].

B. Spatial correlations at equilibrium

Figures 1–3 depict the spatial correlation of conserved variables, that is, $\langle \delta\rho_j \delta\rho_{j^*} \rangle$, $\langle \delta J_j \delta J_{j^*} \rangle$, and $\langle \delta E_j \delta E_{j^*} \rangle$, where j^* is located at the center of the domain.

These figures show results computed by the MacCormack, PPM, and RK3 schemes, along with the theoretical values of the correlations (see Appendix A) and molecular
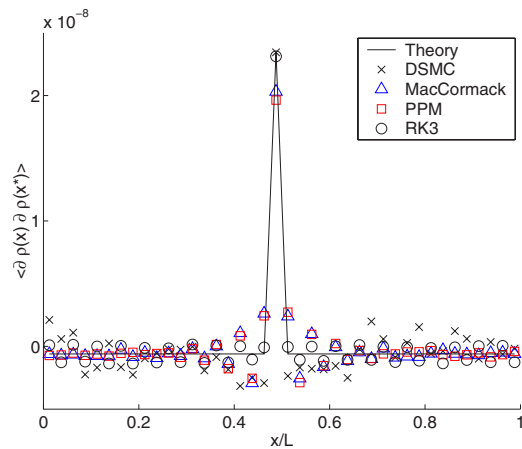
FIG. 1. (Color online) Spatial correlation of density fluctuations. Solid line is $\langle \delta\rho_i \delta\rho_j \rangle = \langle \delta\rho^2 \rangle \delta_{i,j}^K$ [see Eqs. (A2) and (A3)].

FIG. 3. (Color online) Spatial correlation of energy fluctuations. Solid line is $\langle \delta E_i \delta E_j \rangle = \langle \delta E^2 \rangle \delta_{i,j}^K$ [see Eqs. (A5) and (A7)].

simulation data (see Appendix B). For the MacCormack and PPM schemes the spatial correlations of density fluctuations and energy fluctuations have significant spurious oscillations near the correlation point (see Figs. 1 and 3). All three schemes do well in reproducing the expected correlations of momentum fluctuations. Figure 4 depicts $\langle \delta\rho_j \delta J_{j*} \rangle$, which has a theoretical value of zero since the net flow is zero; all three schemes correctly reproduce this result.

Detailed studies of the RK3 scheme show that the method is first-order accurate in t for predicting variances in momentum and energy. The density fluctuations do not appear to improve under temporal refinement; however, the measured errors are only slightly larger than the estimated error bar from the sampling. Spatial accuracy, tested by measuring L^1 norms of $\langle \delta\rho_j \delta\rho_{j*} \rangle$ at various resolutions, showed first order convergence in x.

C. Time correlations at equilibrium

The time correlation of density fluctuations is of interest because its temporal Fourier transform gives the spectral density, which is measured experimentally from light scatter-

ing spectra [53,54]. From the LLNS equations, this time correlation can be written as

$$
\frac{\langle \delta\rho(w,t)\delta\rho(w,t+\tau)\rangle}{\langle \delta\rho^2(w,t)\rangle} = \left(1 - \frac{1}{\gamma}\right)\exp\{-w^2 D_T \tau\}
$$
$$
+ \frac{1}{\gamma}\exp\{-w^2\Gamma\tau\}\cos(c_s w\tau)
$$
$$
+ \frac{3\Gamma - D_v}{\gamma^2 c_s}w\exp\{-w^2\Gamma\tau\}\sin(c_s w\tau),
$$
$$
(7)
$$

where $w = 2\pi n/L$ is the wave number, $\gamma = c_p/c_v$ is the ratio of specific heats, $D_T = \kappa/\bar{\rho}c_v$ is the thermal diffusivity, $D_v = \frac{4}{3}\eta/\bar{\rho}$ is the longitudinal kinematic viscosity, c_s is the sound speed, and $\Gamma = \frac{1}{2}[D_v + (\gamma - 1)D_T]$ is the sound attenuation coefficient.

In our numerical calculations the density is represented by cell averages $\rho_i, i = 1, \ldots, M_c$, and the time correlation is estimated from the mean of N samples,
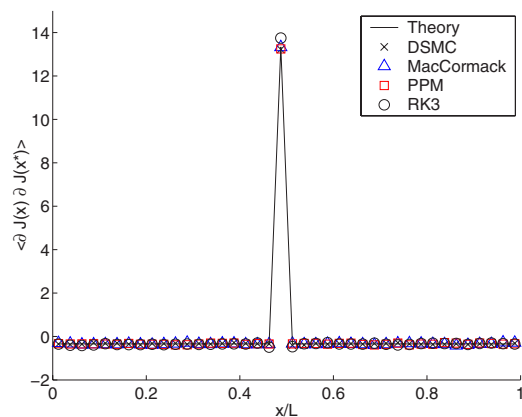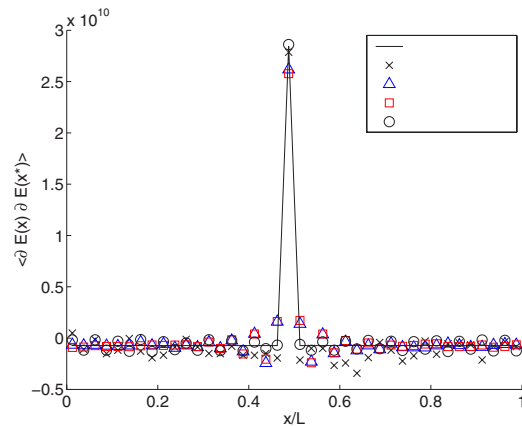

FIG. 2. (Color online) Spatial correlation of momentum fluctuations. Solid line is $\langle \delta J_i \delta J_j \rangle = \langle \delta J^2 \rangle \delta_{i,j}^K$ [see Eqs. (A4) and (A6)].
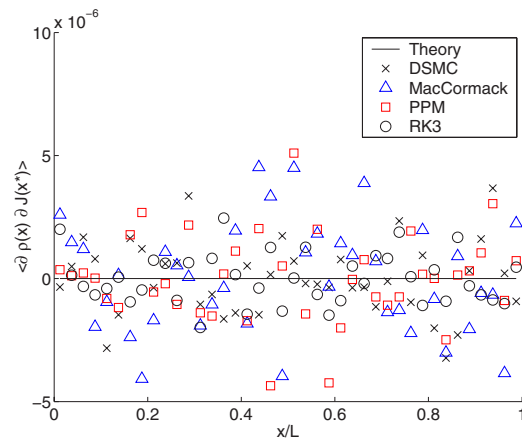

FIG. 4. (Color online) Spatial correlation of density-momentum fluctuations.
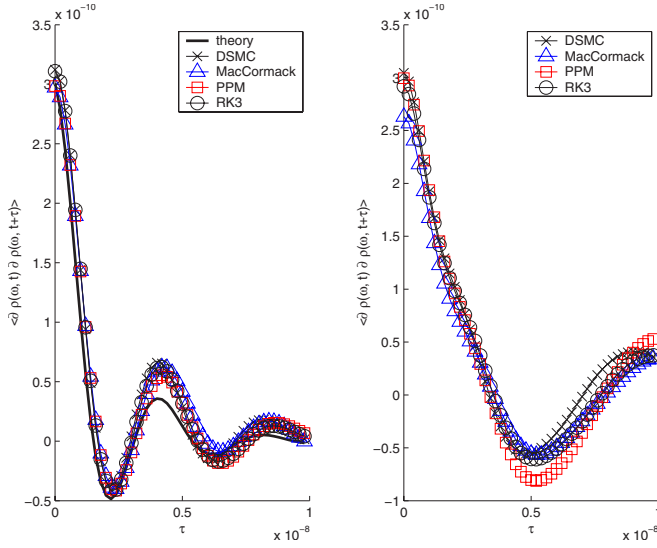
FIG. 5. (Color online) Time correlation of density fluctuations for equilibrium problem, on a periodic domain (left panel) and a domain with specular wall boundaries (right panel).

$$\langle \delta\rho(w,t)\,\delta\rho(w,t+\tau)\rangle_N = \frac{1}{N}\sum_{\text{samples}}^{N} R(t)R(t+\tau)$$

with

$$R(t) = \frac{1}{M_c}\sum_{i=1}^{M_c}\rho_i\,\sin(2\pi n x_i/L).$$

We have

$$\langle \delta\rho(w,t)\,\delta\rho(w,t+\tau)\rangle = \lim_{N\to\infty}\langle \delta\rho(w,t)\,\delta\rho(w,t+\tau)\rangle_N.$$

From the above we find the normalization of the theoretical result may be expressed as

$$\langle \delta\rho^2(w,t)\rangle = \langle R(t)^2\rangle$$
$$= \frac{1}{M_c^2}\sum_{i=1}^{M_c}\sum_{j=1}^{M_c}\langle \delta\rho_i\delta\rho_j\rangle\sin\left(\frac{2\pi n x_i}{L}\right)\sin\left(\frac{2\pi n x_j}{L}\right)$$
$$= \frac{\langle \delta\rho^2\rangle}{2M_c}.$$

We restrict our attention to the lowest wave number (i.e., $n = 1$) because for the system sizes we consider the theoretical result, Eq. (7), is not accurate at short wavelengths due to nonhydrodynamic (mean free path scale) corrections.

In the left-hand panel of Fig. 5, we present time correlation results from our equilibrium problem on a periodic domain. We compare results from the MacCormack, PPM, and RK3 methods with the theoretical time correlation, Eq. (7), and with molecular simulation data (see Appendix A). We find reasonable agreement among all the results, up to the time when a sound wave has crossed the system ($\approx 4\times10^{-9}$ s). Due to finite size effects the theory is only

accurate for short times but the agreement among the numerical PDE schemes and DSMC molecular simulation is good.

The right-hand panel of Fig. 5 shows time correlation results for the equilibrium problem on a domain with thermal walls rather than periodic boundaries; we find good agreement for this problem as well, at least for times less than the sound crossing time. For later times, the time correlation is sensitive to the acoustic impedance of the thermal wall. For this case, MacCormack underpredicts the correlation at early time while PPM shows significant deviation near $t=5 \times10^{-8}$. Both MacCormack and the RK3 scheme deviate somewhat from DSMC at late time. Overall, however, the RK3 scheme captures the temporal correlation better than either of the other two PDE schemes.

IV. NUMERICAL TESTS—NONEQUILIBRIUM

The results from the section above indicate that of the three stochastic PDE schemes, the third-order Runge-Kutta method (RK3) consistently outperforms the other two schemes. In this section we consider two more numerical tests, spatial correlations in a temperature gradient and diffusion of a standing shock wave, but restrict our attention to the RK3 scheme, comparing it with DSMC molecular simulations.

A. Spatial correlations in a temperature gradient

In the early 1980s, a variety of statistical mechanics calculations predicted that a fluid under a nonequilibrium constraint, such as a temperature gradient, would exhibit long-range correlations of fluctuations [55,56]. Furthermore, quantities that are independent at equilibrium, such as density and momentum fluctuations, also have long-ranged correlations. These predictions were qualitatively confirmed by light scattering experiments [57], yet the effects are subtle and difficult to measure accurately in the laboratory. Molecular simulations confirm the predicted correlations of nonequilibrium fluctuations for a fluid subjected to a temperature gradient [29,58] and to a shear [59].

We consider a system similar to that of Sec. III C but with a temperature gradient. Specifically, the boundary conditions are thermal walls at 273 and 819 K. This nonequilibrium state is extreme, with a temperature gradient of millions of degrees per centimeter, yet it is accurately modeled by DSMC, which was originally developed to simulate strong shock waves.

Figure 6 shows the correlation of density and momentum fluctuations measured in an RK3 culation and by DSMC simulations. The two sets of data are in good agreement and are in agreement with earlier work on this problem [29,58]. The major discrepancy is the underprediction of the negative peak correlation near j^*. Extensive tests suggest that this effect is hard to capture with a continuum solver because of the tension between variance reduction and spatial correlations in computing the mass flux at cell edges from cell-centered data.
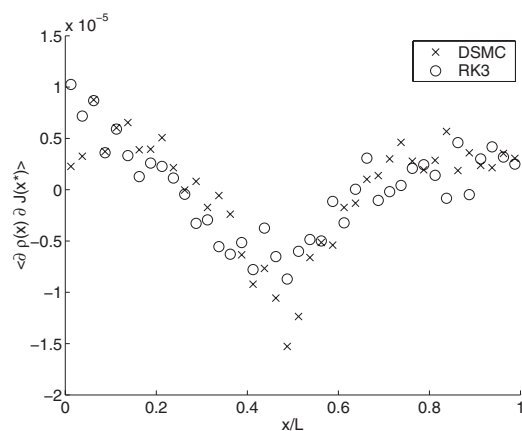
FIG. 6. Spatial correlation of density and momentum fluctuations for a system subjected to a temperature gradient. Compare with Fig. 4.

B. Random walk of a standing shock

In our final numerical study we consider the random walk of a standing shock wave due to spontaneous fluctuations. Shock diffusion is well-known in other particle simulations, such as shock tube modeling by DSMC, which must correct for the drift when measuring profiles for steady shocks [60]. The general problem has been also been analyzed for simple lattice gas models [42,61–64].

Mass density and temperature on the right-hand side (RHS) of the shock are given the same values as in our equilibrium problem; values of density and temperature on the left-hand side (LHS) are derived from the Rankine-Hugoniot relations. The velocity on both sides of the shock are specified to satisfy the Rankine-Hugoniot conditions and to make the unperturbed shock wave stationary in the computational domain. We consider shocks of three different strengths, Mach number (Ma) Ma 2, Ma 1.4, and Ma 1.2 (see Table III). The boundary treatment consists of infinite reservoirs with the same states as the initial conditions. For this

TABLE III. System parameters (in cgs units) for simulations of a standing shock, Ma 2.0.

System length	5×10^{-4}
Reference mean free path	6.26×10^{-6}
System volume	7.84×10^{-16}
Time step	1.0×10^{-12}
Number of cells	160
Mach number	2.0
RHS mass density	1.78×10^{-3}
LHS mass density	4.07×10^{-3}
RHS velocity	$-61\,562$
LHS velocity	$-26\,933$
RHS temperature	273
LHS temperature	567
RHS sound speed	30 781
LHS sound speed	44 373

test problem we use a longer computational domain, in order to capture (unlikely) shock drift of several standard deviations.

Here we focus on the variance of the shock location as a function of time. We define a shock location for density, $\sigma_\rho(t)$ by fitting a Heaviside function to the integrated density, i.e.,

$$\int_{-L/2}^{\sigma(t)} \rho_L dx + \int_{\sigma_\rho(t)}^{L/2} \rho_R dx = \int_{-L/2}^{L/2} \rho(x,t) dx.$$

Solving for $\sigma_\rho(t)$ gives

$$\sigma_\rho(t) = L \frac{\bar{\rho}(t) - (1/2)(\rho_L + \rho_R)}{\rho_L - \rho_R},$$

where $\bar{\rho} = L^{-1} \int_{-L/2}^{L/2} \rho(x,t) dx$ is the instantaneous average density. The shock location for pressure, σ_P, is analogously defined. We estimate $\sigma_\rho(t)$ and $\sigma_p(t)$ as functions of time from ensembles of 4000 simulations. For the PDE simulations, we initialize with discontinuous shock profiles. One would expect the shock location to fluctuate with a diffusion similar to that of a simple random walk [63], so averaging over ensembles from the same initial state we would expect to find

$$\langle \delta \sigma_\rho^2 \rangle \approx 2\mathcal{D}_\rho t \quad \text{and} \quad \langle \delta \sigma_p^2 \rangle \approx 2\mathcal{D}_p t$$

with shock diffusion coefficients $\mathcal{D}_\rho$ and $\mathcal{D}_p$ that depend on shock strength. Note that this expression for the variance is not accurate at very short times (due to transient relaxation from the initial state) or at very long times (due to finite system size).

Figure 7 shows results for the variance in the shock position from an ensemble of runs versus time. After the initial transients, the slopes are constant with the strongest shocks exhibiting the least drift $[\mathcal{D} \cong (\text{Ma}-1)^{-1}]$ and with σ_ρ and σ_P giving similar diffusion coefficients. DSMC data is initially noisy so it has different initial transients and "diffuses" farther than the PDE. However, after the transients, the DSMC and the RK3 simulations have essentially the same slope, as a function of Mach number. This indicates that the third-order Runge-Kutta scheme is accurately capturing the shock-drift random walk.

V. SUMMARY AND CONCLUDING REMARKS

In this paper we develop and analyze several finite-volume schemes for solving the fluctuating Landau-Lifshitz compressible Navier-Stokes equations in one spatial dimension. Methods based on standard CFD discretizations were found not to accurately represent fluctuations in an equilibrium flow. We have introduced a centered scheme based on interpolation schemes designed to preserve fluctuations combined with a third-order Runge-Kutta (RK3) temporal integrator that was able to capture the equilibrium fluctuations. Further tests for nonequilibrium systems confirm that the RK3 scheme correctly reproduces long-ranged correlations of fluctuations and stochastic drift of shock waves, as verified by comparison with molecular simulations. It is worth emphasizing that the ability of continuum methods to accu-
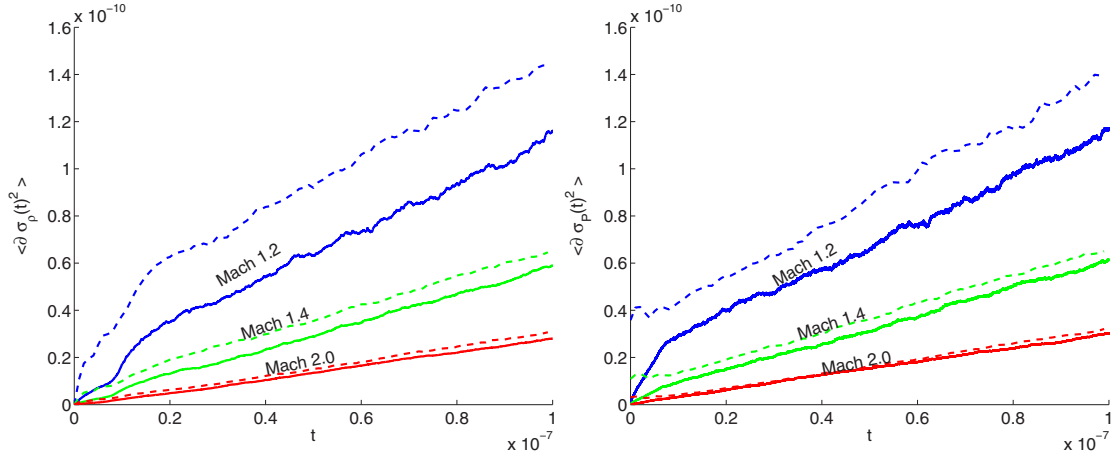
FIG. 7. (Color online) Variance of shock location for mass density profile (left panel, $\langle \delta\sigma_\rho(t)^2 \rangle$) and pressure profile (right panel, $\langle \delta\sigma_P(t)^2 \rangle$). Estimated variances (4000-run ensembles) vs time t for a deterministically steady shock of Mach number 1.2, 1.4, or 2.0. Solid lines are for RK3, dashed lines are from DSMC molecular simulations.

rately capture fluctuations is fairly sensitive to the construction of the numerical scheme. Minor variations in the numerics can lead to significant changes in stability, accuracy, and behavior.

The work discussed here suggests a number of additional studies. Further analysis is needed on the treatment of thermal and reservoir boundary conditions. The methods here can also be extended to three dimensions (for which the stochastic stress tensor is more complex) and we can include concentration as a hydrodynamic variable to allow the methodology to be applied to a number of other flow problems. Finally, we are embedding our new stochastic PDE solver into our existing adaptive mesh and algorithm refinement (AMAR) programs [65]. A stochastic AMAR simulation will not only model hydrodynamic fluctuations at multiple grid scales but will, by incorporating DSMC simulations at the finest level of algorithm refinement, also capture molecular-level physics.

APPENDIX A: EQUILIBRIUM FLUCTUATIONS

At equilibrium the variances of thermodynamic quantities are well known from equilibrium statistical mechanics (Sec. 112 of Ref. [66]). For infinite systems, both conserved and hydrodynamic variables are spatially uncorrelated at equal times. For example,

$$\langle \delta\rho_i(t)\,\delta\rho_j(t) \rangle = \langle \delta\rho^2 \rangle \delta_{i,j}^K. \tag{A1}$$

For conserved variables there is a finite size correction, specifically,

$$\langle \delta\rho_i(t)\,\delta\rho_j(t) \rangle = \left(1 - \frac{1}{M_c}\right)\langle \delta\rho^2 \rangle \delta_{i,j}^K - \frac{1}{M_c}\langle \delta\rho^2 \rangle (1 - \delta_{i,j}^K) \tag{A2}$$

for $i,j=1,\ldots,M_c$, where M_c is the number of cells in the system. This correction may be derived by observing that (i) at equilibrium the system is homogeneous so $\langle \delta\rho_i\delta\rho_j \rangle = A\delta_{ij} + B$ where A, B are constants; (ii) since density is conserved $\Sigma_i\langle \delta\rho_i\delta\rho_j \rangle = 0$ so $A + M_c B = 0$; (iii) in the limit $M_c \to \infty$ we recover the appropriate variance, Eq. (A1). An alternative way to obtain Eq. (A2) is to identify the distribution of particles with the variance and covariance of the multinomial distribution (Sec. 14.5 of Ref. [67]).

The variance of mass density depends on the compressibility (i.e., the equation of state) of the fluid. In general,

$$\langle \delta\rho^2 \rangle = \bar{\rho}^2 \frac{\langle \delta N_c^2 \rangle}{\bar{N}_c^2}, \tag{A3}$$

where $\bar{N}_c$ and $\langle \delta N_c^2 \rangle$ are the mean and variance of the number of particles in a cell. We calculate $\bar{N}_c = \bar{\rho}V_c/m$, where V_c is the volume of a cell and m is the mass of a particle. For an ideal gas N_c is Poisson distributed so $\langle \delta N_c^2 \rangle = \bar{N}_c$ and $\langle \delta\rho^2 \rangle = \bar{\rho}^2/\bar{N}_c$. The more general result is $\langle \delta N_c^2 \rangle = {}_T\rho k_B \bar{T}\bar{N}_c/m$ where ${}_T$ is the isothermal compressibility.

The variances of fluid velocity and temperature in a cell are

$$\langle \delta u^2 \rangle = \frac{k_B\bar{T}}{\bar{\rho}V_c} = \frac{C_T^2}{\bar{N}_c},$$

$$\langle \delta T^2 \rangle = \frac{k_B\bar{T}^2}{c_v\bar{\rho}V_c} = \frac{C_T^2\bar{T}}{c_v\bar{N}_c},$$

where $C_T = \sqrt{k_B\bar{T}/m}$ is the thermal speed (and the standard deviation of the Maxwell-Boltzmann distribution). The covariances are $\langle \delta\rho\,\delta u \rangle = \langle \delta\rho\,\delta T \rangle = \langle \delta u\,\delta T \rangle = 0$.

The variances and covariances of the mechanical densities at equilibrium are

$$\langle \delta\rho\, \delta J \rangle = \bar{\rho}\bar{J}\ _\rho,$$

$$\langle \delta\rho\, \delta E \rangle = \bar{\rho}\bar{E}\ _\rho,$$

$$\langle \delta J^2 \rangle = \bar{J}^2\ _\rho + \bar{\rho}^2 C_T^2\ _u, \tag{A4}$$

$$\langle \delta J\, \delta E \rangle = \bar{J}\bar{E}\ _\rho + \bar{J}\rho C_T^2\ _u,$$

$$\langle \delta E^2 \rangle = \bar{E}^2\ _\rho + \bar{J}^2 C_T^2\ _u + c_v^2 \bar{\rho}^2 \bar{T}^2\ _T, \tag{A5}$$

where $_\rho = \langle \delta\rho^2 \rangle / \bar{\rho}^2$, $_u = \langle \delta u^2 \rangle / C_T^2$, and $_T = \langle \delta T^2 \rangle / \bar{T}^2$. For a dilute gas $_\rho = _u = 1/\bar{N}_c$, and $_T = 2/(3\bar{N}_c)$. Again, corrections must be made for conserved quantities in the case of a finite domain:

$$\langle \delta J_i(t)\, \delta J_j(t) \rangle = \left(1 - \frac{1}{M_c}\right)\langle \delta J^2 \rangle \delta_{i,j}^K - \frac{1}{M_c}\langle \delta J^2 \rangle (1 - \delta_{i,j}^K), \tag{A6}$$

$$\langle \delta E_i(t)\, \delta E_j(t) \rangle = \left(1 - \frac{1}{M_c}\right)\langle \delta E^2 \rangle \delta_{i,j}^K - \frac{1}{M_c}\langle \delta E^2 \rangle (1 - \delta_{i,j}^K). \tag{A7}$$

APPENDIX B: DSMC SIMULATIONS

The algorithms presented here for the stochastic LLNS equations were validated by comparison with molecular simulations. Specifically, we used the direct simulation Monte Carlo (DSMC) algorithm, a well-known method for computing gas dynamics at the molecular scale; see [68,69] for pedagogical expositions on DSMC, [60] for a complete reference, and [70] for a proof of the method's equivalence to the Boltzmann equation. As in molecular dynamics, the state of the system in DSMC is given by the positions and velocities of particles. In each time step, the particles are first moved as if they did not interact with each other. After moving the particles and imposing any boundary conditions, collisions are evaluated by a stochastic process, conserving momentum and energy and selecting the post-collision angles from their kinetic theory distributions. DSMC is a stochastic algorithm but the statistical variation of the physical quantities has nothing to do with the "Monte Carlo" portion of the method. For both equilibrium and nonequilibrium problems DSMC yields the physical spectra of spontaneous thermal fluctuations, as confirmed by excellent agreement with fluctuating hydrodynamic theory [28,29,39] and molecular dynamics simulations [30,71].

In this paper the simulated physical system is a dilute monatomic hard-sphere gas in a rectangular volume with periodic boundary conditions in the y and z directions. The boundary conditions in the x direction are either periodic, specular (i.e., elastic reflection of particles), or a pair of parallel thermal walls. The physical parameters used are presented in Table I. Samples are taken in 40 rectangular cells perpendicular to the x direction.

[1] R. K. Pathria, *Statistical Mechanics* (Butterworth-Heinemann, Oxford, 1996).

[2] G. Karniadakis, A. Beskok, and N. Aluru, *Microflows and Nanoflows: Fundamentals and Simulation* (Springer, New York, 2005).

[3] C. M. Ho and Y. C. Tai, Annu. Rev. Fluid Mech. **30**, 579 (1998).

[4] M. Gad-el-Hak, J. Fluids Eng. **121**, 5 (1999).

[5] B. Alberts, A. Johnson, J. Lewis, M. Raff, K. Roberts, and P. Walter, *Molecular Biology of the Cell*, 4th edition (Garland, New York, 2002).

[6] R. D. Astumian and P. Hanggi, Phys. Today **55** (11), 33 (2002).

[7] G. Oster, Nature (London) **417**, 25 (2002).

[8] R. K. Soong, G. D. Bachand, H. P. Neves, A. G. Olkhovets, H. G. Craighead, and C. D. Montemagno, Science **290**, 1555 (2000).

[9] T. Y. Tsong, J. Biol. Phys. **28**, 309 (2002).

[10] H. G. Craighead, Science **290**, 1532 (2000).

[11] A. van Oudenaarden and S. G. Boxer, Science **285**, 1046 (1999).

[12] J. Bader, R. Hammond, S. Henck, M. Deem, G. McDermott, J. Bustillo, J. Simpson, G. Mulhern, and J. Rothberg, Proc. Natl. Acad. Sci. U.S.A. **96**, 13165 (1999).

[13] C. Van den Broeck, R. Kawai, and P. Meurs, Phys. Rev. Lett. **93**, 090601 (2004).

[14] P. Meurs, C. Van den Broeck, and A. L. Garcia, Phys. Rev. E **70**, 051109 (2004).

[15] M. Moseler and U. Landman, Science **289**, 1165 (2000).

[16] J. Eggers, Phys. Rev. Lett. **89**, 084502 (2002).

[17] W. Kang and U. Landman, Phys. Rev. Lett. **98**, 064504 (2007).

[18] K. Kadau, T. C. Germann, N. G. Hadjiconstantinou, P. S. Lomdahl, G. Dimonte, B. L. Holian, and B. J. Alder, Proc. Natl. Acad. Sci. U.S.A. **101**, 5851 (2004).

[19] K. Kadau, C. Rosenblatt, J. L. Barber, T. C. Germann, Z. Huang, P. Carls, and B. J. Alder, Proc. Natl. Acad. Sci. U.S.A. **104**, 7941 (2007).

[20] B. Nowakowski and A. Lemarchand, Phys. Rev. E **68**, 031105 (2003).

[21] A. Lemarchand and B. Nowakowski, Mol. Simul. **30**, 773 (2004).

[22] L. D. Landau and E. M. Lifshitz, *Fluid Mechanics*, Course of Theoretical Physics Vol. 6 (Addison-Wesley, Reading, 1959).

[23] M. Bixon and R. Zwanzig, Phys. Rev. **187**, 267 (1969).

[24] R. F. Fox and G. E. Uhlenbeck, Phys. Fluids **13**, 1893 (1970).

[25] G. E. Kelly and M. B. Lewis, Phys. Fluids **14**, 1925 (1971).

[26] E. Calzetta, Class. Quantum Grav. **15**, 653 (1998).

[27] P. Español, Physica A **248**, 77 (1998).

[28] A. L. Garcia and C. Penland, J. Stat. Phys. **64**, 1121 (1991).

[29] M. Malek-Mansour, A. L. Garcia, G. C. Lie, and E. Clementi, Phys. Rev. Lett. **58**, 874 (1987).

[30] M. Mareschal, M. Malek-Mansour, G. Sonnino, and E. Kestemont, Phys. Rev. A **45**, 7180 (1992).

[31] A. J. C. Ladd, Phys. Rev. Lett. **70**, 1339 (1993).

[32] N. Sharma and N. A. Patankar, J. Comput. Phys. **201**, 466 (2004).

[33] H. P. Breuer and F. Petruccione, Physica A **192**, 569 (1993).

[34] H. P. Breuer and F. Petruccione, Phys. Lett. A **185**, 385 (1994).

[35] M. Serrano and P. Español, Phys. Rev. E **64**, 046115 (2001).

[36] M. Grmela and H. C. Öttinger, Phys. Rev. E **56**, 6620 (1997).

[37] G. De Fabritiis, P. V. Coveney, and E. G. Flekky, Philos. Trans. R. Soc. London, Ser. A **360**, 317 (2002).

[38] M. Serrano, G. De Fabritiis, P. Español, E. G. Flekkøy, and P. V. Coveney, J. Phys. A **35**, 1605 (2002).

[39] A. L. Garcia, M. Malek-Mansour, G. Lie, and E. Clementi, J. Stat. Phys. **47**, 209 (1987).

[40] F. J. Alexander, A. L. Garcia, and D. M. Tartakovsky, J. Comput. Phys. **182**, 47 (2002).

[41] F. J. Alexander, A. L. Garcia, and D. M. Tartakovsky, J. Comput. Phys. **207**, 769 (2005).

[42] J. B. Bell, J. Foo, and A. L. Garcia, J. Comput. Phys. **223**, 451 (2007).

[43] G. De Fabritiis, R. Delgado-Buscalioni, and P. V. Coveney, Phys. Rev. Lett. **97**, 134501 (2006).

[44] G. De Fabritiis, M. Serrano, R. Delgado-Buscalioni, and P. V. Coveney, Phys. Rev. E **75**, 026307 (2007).

[45] P. Colella, SIAM (Soc. Ind. Appl. Math.) J. Sci. Stat. Comput. **6**, 104 (1985).

[46] P. Colella and P. R. Woodward, J. Comput. Phys. **54**, 174 (1984).

[47] R. E. Miller and E. B. Tadmor, J. Comput.-Aided Mater. Des. **9**, 203 (2002).

[48] P. Colella and H. M. Glaz, J. Comput. Phys. **59**, 264 (1985).

[49] S. Gottleib and C. Shu, Math. Comput. **67**, 73 (1998).

[50] J. Qiu and C. Shu, SIAM J. Sci. Comput. (USA) **26**, 907 (2005).

[51] W. Rumelin, SIAM (Soc. Ind. Appl. Math.) J. Numer. Anal. **19**(3), 604–613 (1982).

[52] P. E. Kloeden and E. Platen, *Numerical Solution of Stochastic Differential Equations* (Springer, New York, 2000).

[53] B. J. Berne and R. Pecora, *Dynamic Light Scattering: With Applications to Chemistry, Biology, and Physics* (Dover, Mineola, 2000).

[54] J. P. Boon and S. Yip, *Molecular Hydrodynamics* (Dover, New York, 1991).

[55] R. Schmitz, Phys. Rep. **171**, 1 (1988).

[56] J. M. Ortiz de Zarate and J. V. Sengers, *Hydrodynamic Fluctuations in Fluids and Fluid Mixtures* (Elsevier Science, New York, 2006).

[57] D. Beysens, Y. Garrabos, and G. Zalczer, Phys. Rev. Lett. **45**, 403 (1980).

[58] A. L. Garcia, Phys. Rev. A **34**, 1454 (1986).

[59] A. L. Garcia, M. Malek-Mansour, G. C. Lie, M. Mareschal, and E. Clementi, Phys. Rev. A **36**, 4348 (1987).

[60] G. A. Bird, *Molecular Gas Dynamics and the Direct Simulation of Gas Flows* (Clarendon, Oxford 1994).

[61] F. J. Alexander, Z. Cheng, S. A. Janowsky, and J. L. Lebowitz, J. Stat. Phys. **68**, 761 (1992).

[62] F. J. Alexander, S. A. Janowsky, J. L. Lebowitz, and H. van Beijeren, Phys. Rev. E **47**, 403 (1993).

[63] P. A. Ferrari and L. R. G. Fontes, Probab. Theory Relat. Fields **99**, 205 (1994).

[64] S. A. Janowsky and J. L. Lebowitz, Phys. Rev. A **45**, 618 (1992).

[65] A. L. Garcia, J. B. Bell, W. Y. Crutchfield, and B. J. Alder, J. Comput. Phys. **154**, 134 (1999).

[66] L. D. Landau and E. M. Lifshitz, *Statistical Physics*, Course of Theoretical Physics, Vol. 5, third ed., part 1 (Pergamon, New York, 1980).

[67] J. F. C. Kingman and S. J. Taylor, *Introduction to Measure and Probability* (Cambridge University Press, Cambridge, England, 1966).

[68] F. J. Alexander and A. L. Garcia, Comput. Phys. **11**, 588 (1997).

[69] A. L. Garcia, *Numerical Methods for Physics*, 2nd ed. (Prentice-Hall, Englewood Cliffs, NJ, 2000).

[70] W. Wagner, J. Stat. Phys. **66**, 1011 (1992).

[71] M. Malek-Mansour, A. L. Garcia, J. W. Turner, and M. Mareschal, J. Stat. Phys. **52**, 295 (1988).